Energy 339 (2025) 139014

Contents lists available at ScienceDirect

Energy

journal homepage: www.elsevier.com/locate/energy

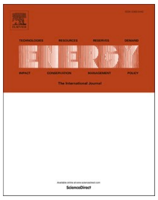

Numerical and surrogate modeling of drying processes in building envelopes under variable climatic conditions

Barbara Ksit [a], Anna Szymczak-Graczyk [b,*], Bożena Orlik-Kożdoń [c], Tomasz Garbowski [d]

[a] Institute of Building Engineering, Faculty of Civil and Transport Engineering, Poznan University of Technology, Piotrowo 5, Poznań, 60-965, Poland
[b] Department of Construction and Geoengineering, Faculty of Environmental and Mechanical Engineering, Poznan University of Life Sciences, Piątkowska 94, Poznań, 60-649, Poland
[c] Department of Building Process and Building Physics, Faculty of Civil Engineering, Silesian University of Technology, Akademicka 2A, 305, Gliwice, 44-100, Poland
[d] Department of Biosystems Engineering, Faculty of Environmental and Mechanical Engineering, Poznan University of Life Sciences, Wojska Polskiego 50, Poznań, 60-627, Poland

ARTICLE INFO

Handling Editor: X Zhao

Keywords:
Moisture content
WUFI 2D
Building envelope moisture
Material drying
Gaussian processes
Principal component analysis

ABSTRACT

Variable climate conditions, including increasingly frequent extreme weather events such as floods and prolonged rainfall, pose a significant challenge to the durability and functionality of building materials. This study analyzes the drying time of multilayer wall partitions subjected to fluctuating moisture loads and different initial moisture levels. A series of hygrothermal simulations was conducted using WUFI software, which solves coupled nonlinear differential equations describing heat and moisture transport in porous materials. The simulations were carried out for various wall configurations commonly used in construction, including autoclaved aerated concrete, ceramic blocks, silicate blocks, and concrete units, using climatic data for Warsaw. Initial moisture levels ranged from air-dry to fully saturated conditions. The results indicate that the drying process strongly depends on the type of material; aerated concrete and silicate blocks showed faster drying rates, while some layers, such as gypsum boards and adhesives, demonstrated significant moisture accumulation during the early stages. Based on these results, a surrogate model was developed using stochastic modeling techniques and principal component analysis (PCA) to compress the simulation data and predict drying times. This model enables rapid estimation of drying periods under various exposure scenarios, supporting improved design and risk assessment after water damage to building envelopes.

1. Introduction

In recent decades, there has been an intensification of extreme weather phenomena, such as heavy rainfall, floods, and prolonged periods of high humidity. These phenomena pose a serious challenge to the durability and functionality of building materials and entire building envelopes. Increased moisture content in the envelope affects energy consumption, which results in higher carbon dioxide emissions [1–4]. Moisture penetrating the material structure can degrade its mechanical, thermal, and aesthetic properties, and it can also promote the growth of microorganisms such as molds and fungi [5–8]. Modern methods of surface renovation require stable moisture conditions in built-in components [9,10].

Traditional methods for assessing moisture-related risks, such as the Glaser method described in the German standard DIN 4108 [11], are based on steady-state assumptions and do not account for dynamic climatic changes or nonlinear processes in porous materials [12–14]. In response to these limitations, advanced numerical methods have been developed in recent years, such as the WUFI 2D software [15], which allows the simulation of coupled heat and moisture transport under transient conditions.

The method used in this study is based on the solution of coupled nonlinear partial differential equations that describe simultaneous heat and moisture transport in capillary-porous building materials [16–18]. The model accounts for vapor diffusion in air, thermal conduction in solids, capillary water transport, and latent heat effects associated with phase change [19–21]. A two-dimensional, transient model was adopted, incorporating sorption, desorption, and redistribution of moisture

---

* Corresponding author.
E-mail addresses: barbara.ksit@put.poznan.pl (B. Ksit), anna.szymczak-graczyk@up.poznan.pl (A. Szymczak-Graczyk), bozena.orlik-kozdon@polsl.pl (B. Orlik-Kożdoń), tomasz.garbowski@up.poznan.pl (T. Garbowski).

https://doi.org/10.1016/j.energy.2025.139014
Received 15 June 2025; Received in revised form 24 September 2025; Accepted 22 October 2025
Available online 24 October 2025

within individual layers of the envelope [22–24]. The simulations were conducted using climate data that included, among others, variable rainfall, ambient humidity, external temperature, and solar radiation. These calculations were performed using the specialized WUFI 2D software [15], which implements the described physical model and allows the inclusion of real meteorological data for the specified location.

However, despite its high accuracy, numerical simulation is time-consuming and computationally expensive, which limits its applicability in engineering practice, especially for multi-scenario or optimization analyses. In response to these challenges, model order reduction techniques such as Principal Component Analysis (PCA) and stochastic process modeling have become increasingly popular, enabling the construction of surrogate models. These models provide fast and efficient predictions of system behavior based on a limited set of input parameters, which is especially useful in the context of design, risk assessment, and remediation planning.

In particular, Gaussian Process Regression (GPR) has proven to be a highly effective surrogate modeling tool, capable of capturing nonlinear input–output relationships while providing uncertainty estimates. Its application in engineering extends to both direct prediction and inverse identification problems, as demonstrated in previous works combining GPR with dimensionality reduction techniques like PCA or POD [25,26]. Effective surrogate modeling requires not only robust training but also appropriate sampling strategies in the input space to ensure good generalization properties. Buljak and Garbowski [27] discussed the importance of optimal space-filling designs in the context of reduced-order models using POD and radial basis functions (RBF), emphasizing the trade-off between accuracy and computational cost. The POD-RBF methodology has been extensively described and validated in inverse problems by Buljak [28], including its mathematical foundations, interpolation properties, and sensitivity to noise. Earlier work by Garbowski [29] also underlined the benefits of stochastic model reduction in inverse problems, supporting its integration into modern engineering workflows.

The aim of this study is to analyze the drying process of building partitions made of different materials—such as autoclaved aerated concrete, ceramic blocks, silicate blocks, and concrete—under variable climatic conditions typical for the Warsaw region. A series of numerical simulations was performed using WUFI 2D [15], considering different initial moisture levels and operational conditions. Based on the obtained results, a surrogate model using principal component analysis and stochastic modeling was developed to quickly estimate drying times for various exposure scenarios. The proposed approach serves as a tool to support design processes and moisture risk management in buildings.

Compared to traditional approaches such as the Glaser method, empirical drying curves, or static drying tables, the proposed modeling framework offers a significant improvement in both predictive accuracy and flexibility. While classical methods often rely on steady-state assumptions and simplified thermal-moisture interactions, our method captures transient, multidimensional hygrothermal effects and allows adaptation to varying climatic and material scenarios. Moreover, once trained, the surrogate model provides instant predictions with quantified uncertainty, enabling use in real-time decision-making, risk assessment, or optimization tasks.

2. Materials and methods

2.1. Laboratory investigations

The materials used in the masonry constructions typically exhibit a capillary-porous structure [30,31]. The pore sizes within the microstructure of small-sized masonry elements vary widely, from nanometers to millimeters [32,33]. These pores appear in various forms and geometries. A key indicator of a porous material's ability to absorb moisture is its effective porosity, defined as the ratio of the volume of open pores to the total volume of the considered sample [30,34].

Moisture content testing is one of the most frequently performed measurements to determine material properties and the moisture state of building envelopes. Moisture content is described as the relative amount of water in the material [35], and can be expressed as either mass moisture or volumetric moisture. In this study, mass moisture was determined using the following relation:

$$w_m = \frac{m_w - m_d}{m_d} \cdot 100\ [\%] \tag{1}$$

where:

m_w – mass of the sample in the wet state [kg],
m_d – mass of the sample in the dry state [kg].

Test methods for measuring moisture content vary in their level of invasiveness. Direct measurement techniques rely on readings from appropriate measuring equipment, based on the known relationship between the measured value and other physical quantities [36,37]. In this study, the classification of testing methods follows the categories listed in the PN-EN 16682:2017 standard [38], which distinguishes between absolute, relative, and safety-critical measurement methods. The review of available measurement protocols revealed inconsistencies and gaps in methodological guidelines, introducing the potential for unintentional error. To obtain reliable measurements, at least 9 repeated readings per partition were performed using the same device.

The tested wall configurations consisted of small-format masonry units with a single layer of gypsum plasterboard, attached using adhesive mortar dabs. Cement-lime mortar with a volumetric ratio of 2:0.5:8 (hydrated lime: CEM I 32.5R Portland cement: 0–2 mm sand) was used to build the walls, along with market-available porous materials made from regular concrete, autoclaved aerated concrete (AAC), silicates, and perforated ceramics Each wall prepared for the experiment was 24 cm thick, 75 cm high and 100 cm long (Fig. 1).

After 28 days of curing at 25.0 ± 1.5 °C and 45.0 ± 2.5 % relative humidity (conditions were monitored using temperature and humidity dataloger), the walls were exposed to moisture loading using tap water for 30 days. Moisture content was then measured under ambient conditions of 17.8 ± 1.5 °C and 40.1 ± 2.0 % relative humidity. All samples were watered with the same amount of water on the same day, at the same time, with the same water flow rate, the same water temperature and the same environmental conditions.

2.2. Numerical simulations

Drying time estimation for the analyzed wall systems was performed using WUFI 2D software [15]. The program is based on a system of nonlinear partial differential equations that describe unsteady heat and moisture transport in capillary-porous materials. For one-dimensional flow, the transport equations take the form [39–42].

Heat transport:

$$\frac{\partial H}{\partial T}\frac{\partial T}{\partial t} = \frac{\partial}{\partial x}\left(\lambda \frac{\partial T}{\partial x}\right) + h_v \frac{\partial}{\partial x}\left(\frac{\delta_o}{\mu}\frac{\partial p}{\partial x}\right), \tag{2}$$

Moisture transport:

$$\rho_w \frac{\partial u}{\partial \varphi}\frac{\partial \varphi}{\partial t} = \frac{\partial}{\partial x}\left(\rho_w D_w \frac{\partial u}{\partial \varphi}\frac{\partial \varphi}{\partial x}\right) + \frac{\partial}{\partial x}\left(\frac{\delta_o}{\mu}\frac{\partial p}{\partial x}\right), \tag{3}$$

where:

D_w – capillary conductivity coefficient [m^2/s],
H – enthalpy of wet material [J/m^3],
h_v – heat of vaporization [J/kg],
p – partial pressure of water vapor [Pa],
u – moisture content [m^3/m^3],
δ_o – diffusion coefficient of water vapor in air [kg/m·s·Pa],
T – ttemperature [^{o}C],
λ – thermal conductivity coefficient of wet material [W/m·K],
μ – diffusion resistance coefficient of dry materia [–],

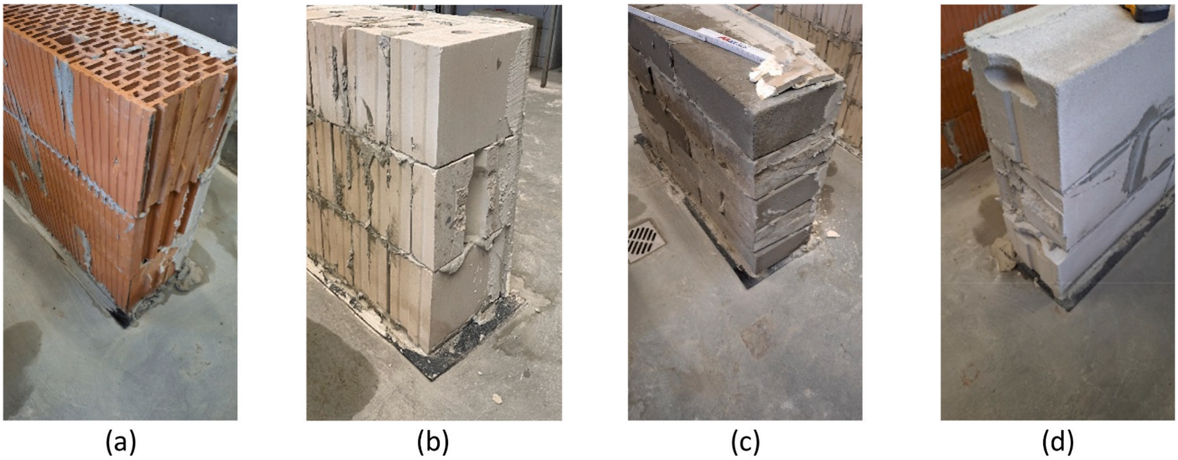

Fig. 1. Wall system models: ceramic block (a), silicate block (b), regular concrete (c), autoclaved aerated concrete – AAC (d).

ρ_w – water density [kg/m^3],
φ – relative humidity [−].

The equations include both liquid and vapor moisture transport mechanisms, as well as the thermal effects of phase transitions. Boundary and initial conditions were defined based on actual climate data for Warsaw (temperature, humidity, solar radiation, wind-driven rain), with simulations carried out for a 3-year period, starting from a fixed moisture loading scenario. The external and internal surface of each wall was subjected to varying climatic conditions.

Different initial moisture conditions were defined for each wall system: from air-dry, through 5 %, 8 %, 12 % mass moisture, up to full saturation. For each configuration, drying profiles were recorded for selected layers: the structural element (e.g., block), mortar, adhesive, and plasterboard.

The simulation outputs—time-dependent moisture content in critical layers—were used to define the drying time, interpreted as the period necessary to reach a near-stable moisture profile. These data served as input for the surrogate model, described in the next section.

The applied heat and moisture transport model accounts for material sorption properties, moisture redistribution capacity, and comprehensive external climate effects, including wind-driven rain.

The analyzed wall configurations are shown in Fig. 1, and the input data along with material properties are summarized in Table 1, Fig. 2a and b.

The calculations were performed using the following assumptions.

- the indoor climate according to *EN 15026* (Fig. 3), – average humidity load, was adopted in accordance with the methodology given in *EN 15026* (Fig. 3b), i.e., the indoor air conditions are obtained by entering the daily outdoor air temperature (based on TMY) into the graph in Fig. 3a; the indoor air humidity level is selected depending on the projected operating mode (low load/normal load/high load),
- external climate for the Warsaw location - a representative city for Poland (the capital) was adopted; the external climate takes into account variable weather conditions such as: temperature, relative humidity, global radiation, solar radiation, driving rain, normal rain; the figure shows the assumed boundary conditions of the external climate (Fig. 4),
- rain load according to ASHRAE 160 [43]: Rain exposure category: medium, building height >10 m < 20 m, rain exposure factor 1.2 [-], rain deposition factor 0.35 [-]
- partition orientation - north direction N,
- thermal resistance $R_{si} = 0.13$ [(m^2 K)/W], $R_{se} = 0.04$ [(m^2 K)/W] [44],
- the outdoor climate of October 1, 2025, at 00:00 was assumed as the initial conditions for all simulations,
- all simulations were conducted over a three-year period from the start date, i.e., until October 1, 2028, at 00:00, with a time step of 1 h,
- the initial moisture content was assumed for an air-dry condition, i.e., for the moisture content of the material at 80 % relative humidity; variant **V_0** (Table 1),
- the analyses also included calculation variants that took into account different material moisture contents: 5 %M (variant **V_1**), 8 %M (variant **V_2**), 12 %M (variant **V_3**), and the saturation state – **V_4** (full saturation of the material pores with water).

2.3. *Mathematical model: PCA and Gaussian Process Regression*

To construct the surrogate model, a two-step procedure was employed. In the first step, Principal Component Analysis (PCA) was used to reduce the dimensionality of the simulation data obtained from WUFI [15]. In the second step, a probabilistic regression model based on Gaussian Process Regression (GPR) was developed to predict the drying time under various initial conditions.

Table 1
Physical properties of the materials used in the study.

Material		Thermal conductivity coefficient λ [W/m·K]	Diffusion resistance coefficient μ[−]	Initial moisture content		Volumetric density ρ [kg/m^3]	Porosity of the material ε [m^3/m^3]
				[kg/m^3]	[%M]		
Wall material	silicate block	1.0	34	27.5	1.50	1830	0.35
	ceramic block	0.10	16	11	1.83	600	0.77
	regular concrete block	1.60	92	53	2.41	2200	0.18
	autoclaved aerated concrete block	0.13	15	15	2.31	650	0.74
Plasterboard adhesive		0.54	31	8.4	0.60	1395	0.46
Cement-lime mortar		0.60	50	25.7	1.37	1880	0.28
Plasterboard		0.20	8.3	6.30	0.74	850	0.65

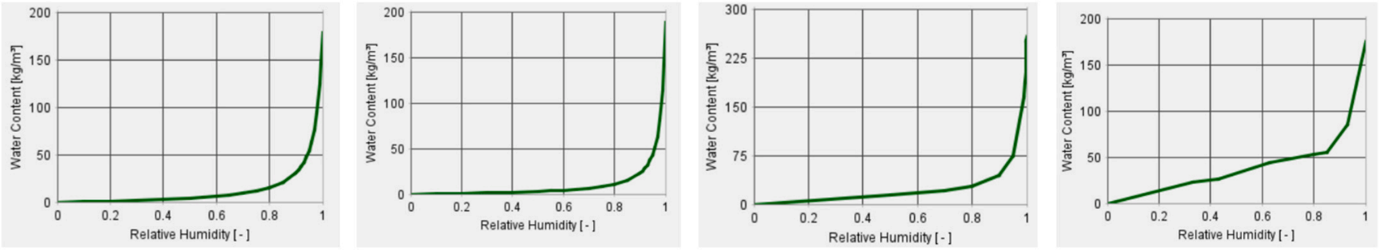

(a) (b) (c) (d)

Fig. 2a. Moisture storage function/sorption curve for autoclaved aerated concrete block (a), ceramic block (b), silicate block (c), regular concrete block (d).

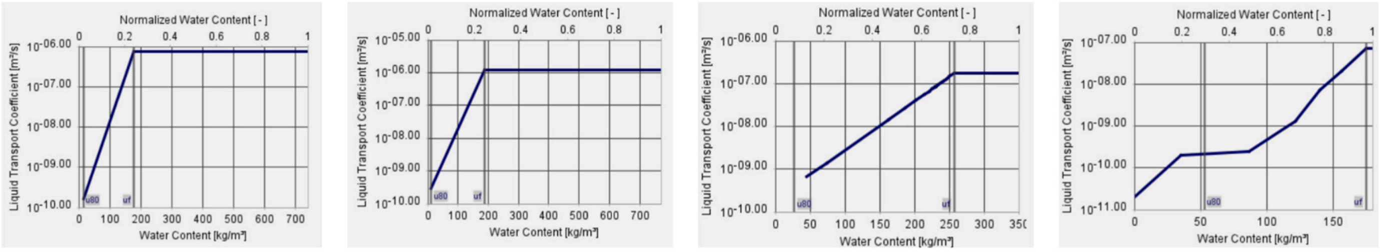

Fig. 2b. Liquid transport coefficient/redistribution for autoclaved aerated concrete block (a), ceramic block (b), silicate block (c), regular concrete block (d).

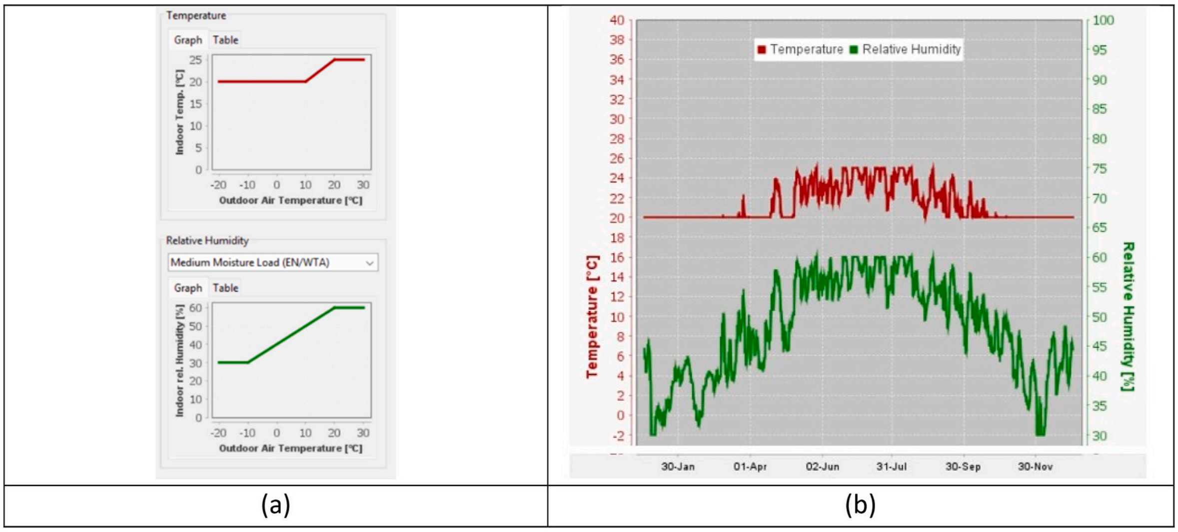

Fig. 3. Indoor climate model: (a) average daily temperature and humidity of indoor air, (b) obtained indoor climate model for the climatic conditions of the city of Warsaw and normal moisture load.

Dimensionality reduction using PCA.

Let $u(x,t) \in R^n$ denote the moisture (or temperature) distribution at a given point in time t. For m time samples, the data matrix is defined as:

$$\mathbf{U} = [\mathbf{u}(t_1), \mathbf{u}(t_2), \ldots, \mathbf{u}(t_m)] \in R^{n \times m} \tag{4}$$

PCA involves solving the eigenvalue problem for the covariance matrix:

$$\mathbf{C} = \frac{1}{m}\mathbf{U}\mathbf{U}^{\top}, \mathbf{C}\mathbf{V} = \mathbf{V}\mathbf{\Lambda} \tag{5}$$

where $\mathbf{V} = [v_1, v_2, \ldots, v_r]$ are the principal components and Λ the corresponding eigenvalues. Each distribution $u(ti)$ can be approximated as:

$$\mathbf{u}(t_i) \approx \sum_{k=1}^{r} a_k(t_i)\mathbf{v}_k \quad or \quad \mathbf{U} \approx \mathbf{V}_r\mathbf{A}, \tag{6}$$

where $\mathbf{A} \in R^{r \times m}$ contains the projection coefficients onto the reduced basis.

After dimensionality reduction using PCA, the surrogate model was trained using Gaussian Process Regression (GPR), a non-parametric, probabilistic approach suitable for problems with limited but informative data. The target variable is the drying time, defined as the time required to reach a quasi-equilibrium moisture level at key locations in the wall.

Input space and training data.

Each input vector $x \in R^d$ combines:

- material properties (e.g. porosity, thermal conductivity, vapor diffusion resistance),
- initial moisture level (in kg/m^3),
- geometric features of the wall (e.g. layer thicknesses),

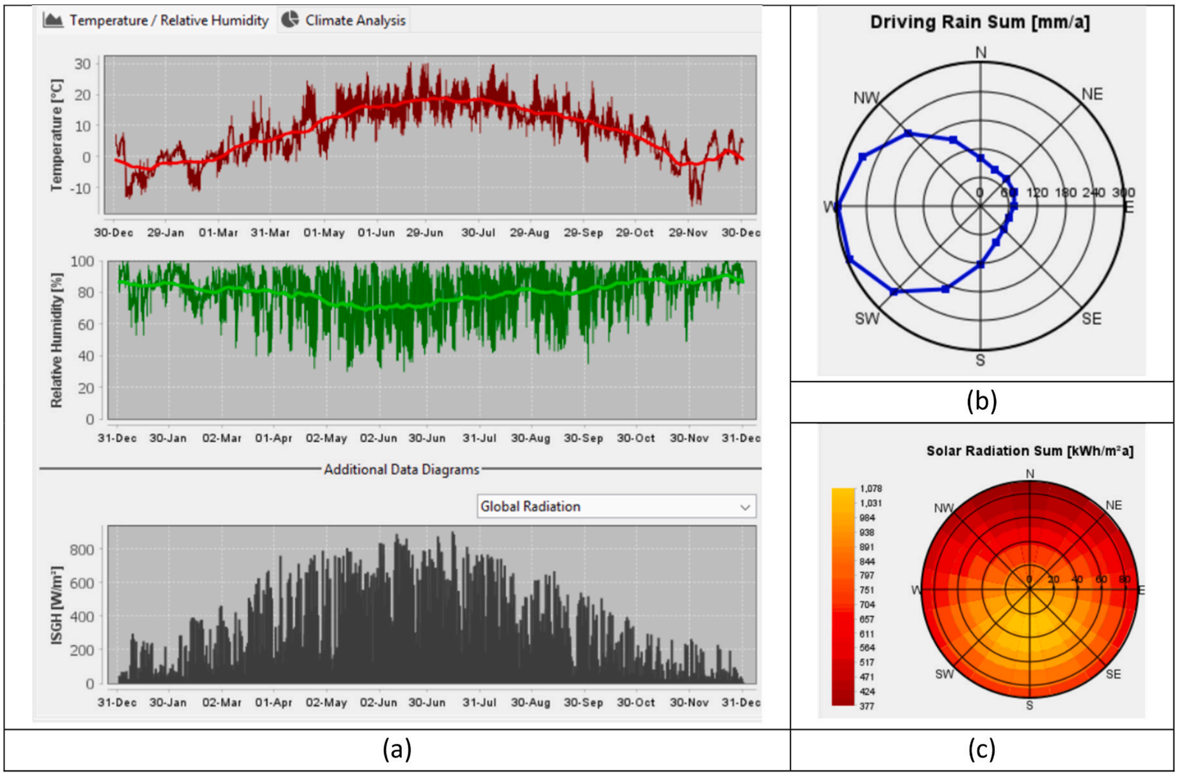

Fig. 4. Outdoor climate parameters: (a) temperature, relative humidity, global radiation, (b) driving rain, (c) solar radiation.

- and compressed climate data (the PCA transformation was applied to hourly climatic data (temperature, relative humidity, rainfall, solar radiation) collected over 3 years for Warsaw, and the first 10 principal components capturing over 95 % of total variance were retained).

The training set $\{x_i, y_i\}_{i=1}^{N}$ was built using results from 24 full simulations, with synthetic data augmentation through interpolation for additional configurations. Synthetic data for surrogate model training were generated using cubic spline interpolation between discrete simulation results for the air-dry state (steady state) up to full water saturation.

The GPR model assumes that the latent function $f(x)$ follows a Gaussian process:

$$f(x) \sim GP(m(\mathbf{x}), k(\mathbf{x}, \mathbf{x}')), \tag{7}$$

where.

- $m(\mathbf{x})$ is the mean function, typically set to zero,
- $k(\cdot,\cdot)$ is the covariance function (kernel) defining the similarity between data points.

Several kernel types were evaluated. The most effective in this study was the squared exponential (RBF) kernel, defined as:

$$k_{RBF}(\mathbf{x}, \mathbf{x}') = \sigma_f^2 \exp\left(-\frac{1}{2l^2}|\mathbf{x} - \mathbf{x}'|^2\right) \tag{8}$$

where.

- σ_f^2 is the signal variance,
- l is the characteristic length scale.

Alternative kernels (tested for completeness) included.

- Matérn kernel (for rougher functions):

$$k_{Matern}(\mathbf{x}, \mathbf{x}') = \frac{\sigma_f^2 2^{1-\nu}}{\Gamma(\nu)} \left(\frac{\sqrt{2\nu}\,|\mathbf{x} - \mathbf{x}'|}{l}\right)^{\nu} K_\nu\left(\frac{\sqrt{2\nu}|\mathbf{x} - \mathbf{x}'|}{l}\right) \tag{9}$$

with $\nu = \frac{3}{2}$ or $\nu = \frac{5}{2}$,

- Rational quadratic kernel (effectively a sum of RBF kernels with different length-scales):

$$k_{RQ}(\mathbf{x}, \mathbf{x}') = \sigma_f^2 \left(1 + \frac{|\mathbf{x} - \mathbf{x}'|^2}{2\alpha l^2}\right)^{-\alpha} \tag{10}$$

The kernel parameters $\theta = \{\sigma_f, l, \sigma_n\}$ were learned by maximizing the log marginal likelihood:

$$\log p(\mathbf{y}|\mathbf{X}, \theta) = -\frac{1}{2}y^\top \left(\mathbf{K} + \sigma_n^2\mathbf{I}\right)^{-1} y - \frac{1}{2}\log\left(\det\left(K + \sigma_n^2 I\right)\right) - \frac{n}{2}\log 2\,\pi \tag{11}$$

This optimization was performed using the L-BFGS-B algorithm, which is well-suited for problems with continuous, bounded parameters. The L-BFGS-B optimization of kernel hyperparameters used initial values of 1.0 for all parameters, bounded within [1e-2, 1e3], and terminated when relative objective function change was less than 1e-6 or after 1000 iterations.

The final trained GPR model allows not only to predict the drying time $\hat{y}_*$ for a new input x_*, but also to quantify the uncertainty:

$$y_* = \mathbf{k}_*^\top \left(\mathbf{K} + \sigma_n^2\mathbf{I}\right)^{-1} \mathbf{y} \tag{12}$$

$$Var[y_*] = k(\mathbf{x}_*, \mathbf{x}_*) - \mathbf{k}_*^\top \left(\mathbf{K} + \sigma_n^2\mathbf{I}\right)^{-1} \mathbf{k}_* \tag{13}$$

This capability is particularly valuable for risk-aware engineering decision-making.

3. Results and discussion

3.1. Results of mass moisture content measurements

To examine the internal structure of the analyzed wall materials and verify potential material inhomogeneity, scanning electron microscopy (SEM) was performed using a QUANTA 250 microscope (Fig. 5a–d).

SEM observations revealed significant grain variability in silicate, AAC, and regular concrete samples, whereas the ceramic sample showed a uniform grain structure. The silicate block images showed irregularly shaped inclusions and agglomerates of fine particles. In the regular concrete sample, large inclusions of both irregular and spherical shapes were identified. The AAC sample exhibited characteristic spherical voids, indicating air bubbles formed during the foaming process. The SEM images (Fig. 5a–d) suggest differing water absorption potentials due to the distinct pore structures of the analyzed materials.

Moisture content measurements were performed using both destructive (direct) and non-destructive (indirect) methods. Electrical moisture meters were used, including dielectric, resistive, and microwave types, alongside gravimetric analysis. Core samples for the destructive method were taken using a 20 mm diameter drill, extracted at depths of approximately 5 cm and 10 cm. The moisture content was measured using a Trotec T610 microwave meter, a Brennenstuhl MD resistive meter, and a Gann dielectric meter (Fig. 6). Measurements were carried out at different wall heights: 10 cm, 40 cm, and 60 cm.

Due to the large volume of data, Table 2 presents moisture content results at heights of 60 cm and 10 cm for ceramic blocks, autoclaved aerated concrete (AAC), silicate blocks, and concrete blocks.

The analysis included correlation of the results and guidelines provided by the moisture meter manufacturers. Interpretation was based on average readings in accordance with the instructions provided with the measurement devices. In order to determine the actual mass moisture content of the tested partition, control measurements were carried out using the invasive method (MN). The tested masonry was damp up to the saturation level. Among the tested materials, ceramic hollow block, characterized by a fine-pored structure, exhibited the highest saturation. It should be noted that the maximum values of saturation of this material are achieved under vacuum conditions, where air is evacuated from the pore network, allowing the material to absorb water up to its total open porosity. This process is used to define a theoretical upper limit of saturation, which exceeds the levels achievable under natural capillary absorption. In our study, this fully saturated state is introduced as a boundary scenario to assess drying dynamics under extreme conditions. The tests conducted on samples taken using different methods showed significant variability in results even within a single wall layer.

After conducting a series of measurements using non-invasive devices, it was found that many commercially available meters have a limited measurement range and restricted applicability, often being suitable only for specific materials. The interpretation of the obtained results was based on determining the moisture condition of the masonry (Table 3).

Microwave-based indirect measurements using the Trotec T610 m showed that, according to the manufacturer's moisture classification scale, all tested materials were classified as "dry." However, it must be noted that such measurements should be calibrated, as the manufacturer states that accurate readings are only valid for materials tested at the RWTH Aachen Institute of Building Research—namely adhesive, screed, and C30/37 concrete [48].

The next measurement, using the MD resistive meter, was based on evaluating electrical resistance between two electrodes in the damp material. This method classified all tested materials as "wet." The uncertainty of resistive moisture meters ranges from 1 % to 10 %, depending on the degree of moisture [49].

Using the Gann dielectric meter with a spherical probe, further measurements were conducted. Based on the readings and the manufacturer's guidelines, the results indicated high moisture levels in concrete and very high moisture in other porous materials.

These findings support existing hypotheses in the literature, which state that "for indirect methods, measurement differences are negligible at high absolute moisture contents, but at lower moisture levels, meters show significant deviations" [35,50]. Moisture measurements were also taken on the surface of the gypsum board in all cases, the measured moisture content was close to zero, ranging from 0.50 to 0.6 %.

Destructive tests on AAC blocks confirmed high moisture levels, while other materials were classified as having either acceptable or elevated moisture levels. As noted by other researchers [51–54], although non-invasive meters are readily available and easy to use, the results they produce are not always reliable. Our study confirms that calibration is essential for such devices, and even results from a single device may vary by 3–4 %.

Moreover, moisture distribution within masonry varies both vertically and horizontally, and non-invasive devices measure moisture at

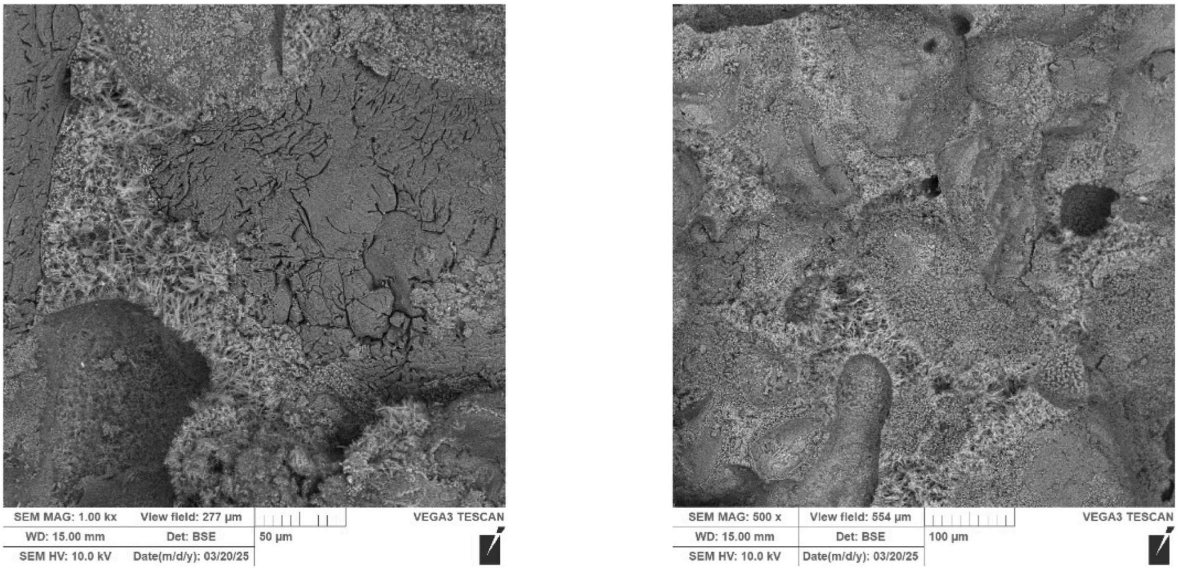

(a) (b)

Fig. 5a. SEM image of the silicate block sample: magnification 50 μm (a), 100 μm (b).

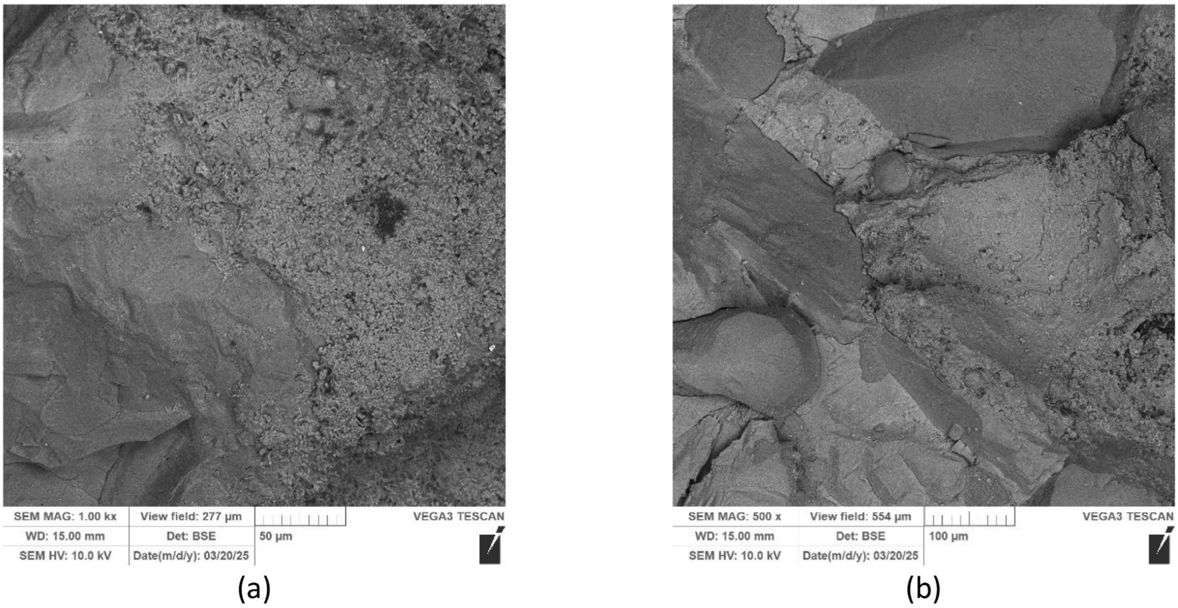

Fig. 5b. SEM image of the regular concrete block sample: magnification 50 µm (a), 100 µm (b).

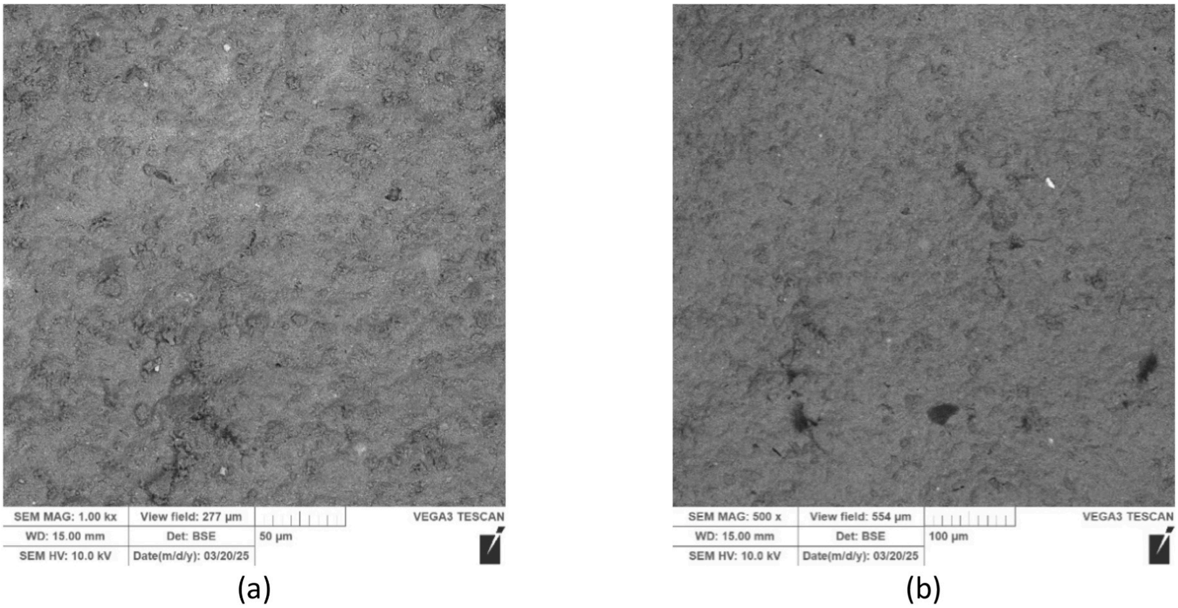

Fig. 5c. SEM image of the ceramic block sample: magnification 50 µm (a), 100 µm (b).

different depths (approx. 1 cm for MD, 4 cm for Gann, and up to 30 cm for T610). In the authors' opinion, indirect measurements are suitable for preliminary assessments, mapping moisture distribution, and monitoring changes over time. However, they should be considered indicative only, as they may significantly differ from destructive method results, which themselves may also be affected by measurement error.

3.2. Results of moisture content variation simulations

The simulation results estimating changes in moisture content over time are presented for areas relevant to both structural integrity and operational performance. For each wall configuration (Fig. 1), a simplified model was created to identify key locations for evaluating moisture variation over the observation period of three years (Fig. 7).

The simulation results are presented as follows.

1. Moisture content variation over a 3-year period for selected areas: 1 (block), 2 (mortar), 3 (adhesive), 4 (gypsum board); additionally, in the gypsum board layer at the interfaces with the adhesive and with the air layer (for the saturated moisture condition), see Fig. 8.
2. Distribution of isopleths on the external surface, internal surface, the surface of the gypsum board in contact with the air gap (installation void), and the block–air interface, shown only for the fully saturated case, see Fig. 9.

The figures present representative graphical results for the wall made of autoclaved aerated concrete (Fig. 8a-d). Additional results obtained through numerical simulations in WUFI 2D [15] are summarized in Tables 4–7.

Fig. 8a-d shows profiles of changes in moisture content in individual layers of autoclaved concrete wall.

Fig. 9a-d shows how the moisture content of the wall components

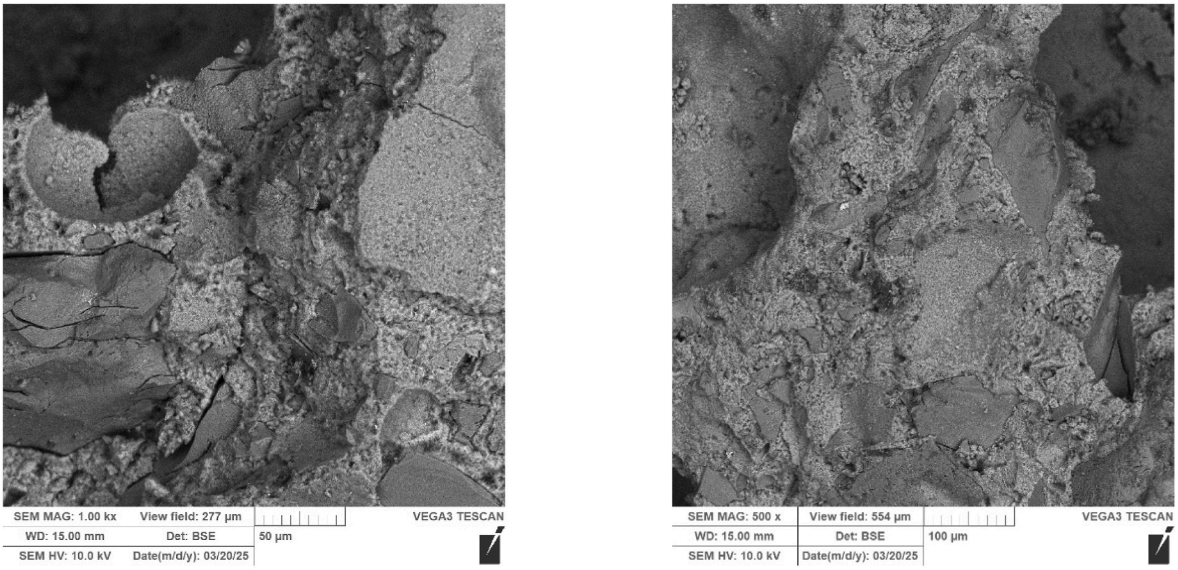

(a) (b)

Fig. 5d. SEM images of autoclaved aerated concrete (AAC) sample: magnification 50 μm (a), 100 μm (b).

(a) (b) (c)

Fig. 6. Indirect moisture measurement using handheld moisture meters: (a) MD, (b) T610, (c) Gann.

Table 2
Moisture measurement results for masonry walls.

	ceramic block	silicate block	regular concrete block	autoclaved aerated concrete block (AAC)
T610 [%]	27.6–37.6	25.9–38.5	34.6–39.3	18–23.9
MD [%]	18.5–19.5	17–20.4	15–19.8	23.5–24
Gann [jtk]	110–118	130–133	98–119	130–136
MN [%]	2.30–2.72	1.51–3.98	1.19–2.01	22.56–23.71

changes over time and how long it takes for the wall to reach moisture equilibrium, i.e., the moisture content in the material at a relative air humidity of 80 % (these values for individual materials are summarized in Table 1). The results in Fig. 9a-d are presented for the full water saturation variant V4.

Analyzing the changes in moisture content over time for different wall models, it is found.

Table 3
Moisture classification system based on five criteria indicating the degree of masonry moisture [45–47].

Degree/ criteria	Moisture (absolute) mass of masonry	Relative humidity of masonry interpretation of requirements (acc. 34,47)	The degree of moisture in the masonry
I	0,0 % - 3,0 %	<20 %	with acceptable moisture
II	3,0 % - 5,0 %	20 %–40 %	with increased moisture
III	5,0 % - 8,0 %	41 %–60 %	moderately humid
IV	8,0 % - 12,0 %	61 %–75 %	heavily humid
V	>12,0 %	>75 %	wet walls

- The qualitative profile of changes in the structural material and mortar shows a clear downward trend (Fig. 8),

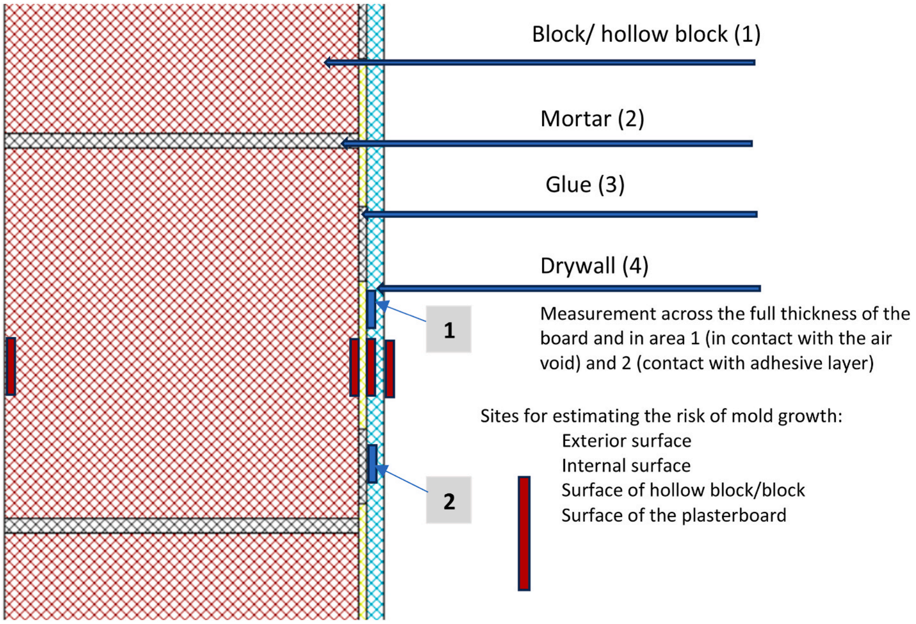

Fig. 7. Section of the wall model with marked measurement points.

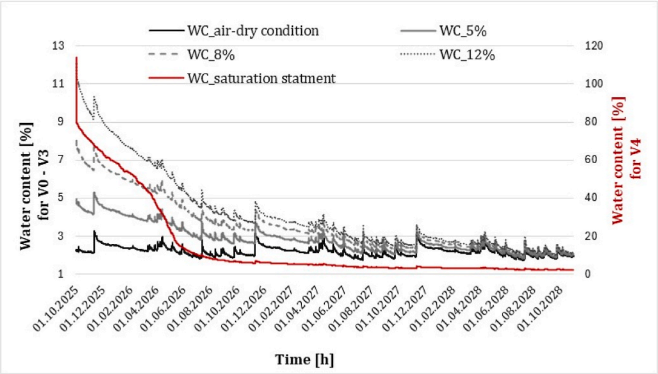

Fig. 8a. Moisture content variation over time for autoclaved aerated concrete block.

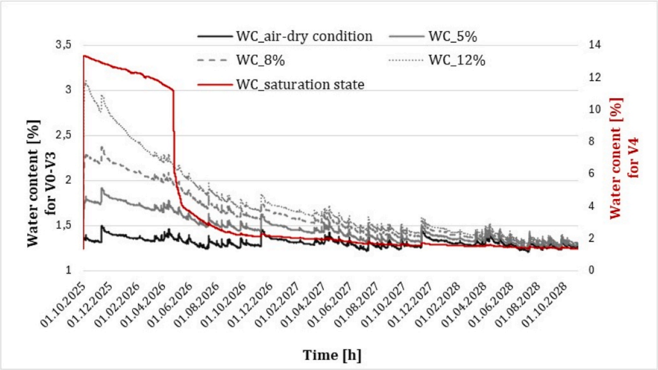

Fig. 8b. Moisture content variation over time for mortar.

- Regardless of the initial moisture level of the structural materials and mortar (5 % to saturation), the moisture change profile shows the same qualitative trend, with quantitative differences up to year 3 (Fig. 8),

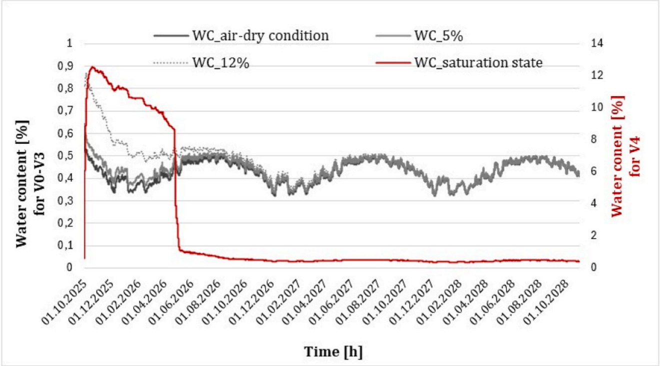

Fig. 8c. Moisture content variation over time for adhesive.

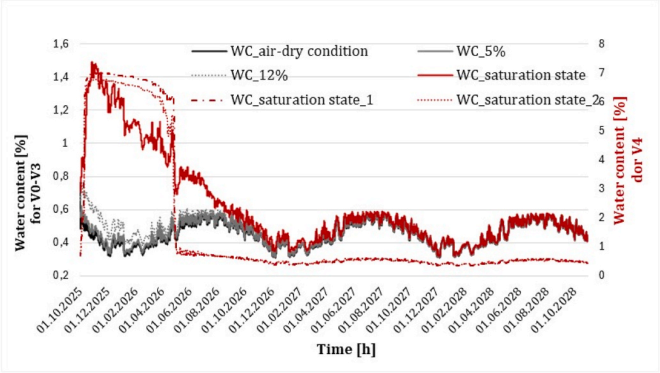

Fig. 8d. Moisture content variation over time for gypsum board.

- Regardless of the preset level of moisture content of the wall's structural material (5 % to the saturated state), most of the water dries out in the first year of operation (Tables 4–7),
- The maximum moisture content of construction materials is determined by their structure (porosity) and water transport capacity (sorption and other hygrothermal functions). The lowest initial

Table 4
Moisture content changes for the wall system made of autoclaved aerated concrete.

Components of the wall system	Initial moisture content	Moisture content during the measurement period [%]			
		October 01, 2025	October 01, 2026	January 01, 2027	October 01, 2028
autoclaved aerated concrete block	Air-dry condition	2.31	2.11	2.06	2.07
	5 %	4.93	2.82	2.29	2.11
	8 %	8.03	3.52	2.52	2.19
	12 %	12.06	4.00	2.68	2.24
	Saturation state	113.85	6.58	3.39	2.47
mortar	Air-dry condition	1.37	1.29	1.28	1.28
	5 %	1.37	1.48	1.34	1.29
	8 %	1.37	1.62	1.41	1.32
	12 %	1,37	1.72	1.45	1.33
	Saturation state	1,37	2.21	1.59	1.39
adhesive	Air-dry condition	0.60	0.42	0.42	0.42
	5 %	0.60	0.43	0.42	0.42
	8 %	0.60	0.44	0.43	0.42
	12 %	0.60	0.45	0.43	0.42
	Saturation state	0,60	0.52	0.44	0.43
gypsum board	Air-dry condition	0.74	0.42	0.42	0.42
	5 %	0.74	0.42	0.42	0.42
	8 %	0.74	0.43	0.42	0.42
	12 %	0.74	0.43	0.42	0.42
	Saturation state	0.74	0.48	0.43	0.42

Table 5
Moisture content changes for the wall system made of ceramic block.

Components of the wall system	Initial moisture content	Moisture content during the measurement period [%]			
		October 01, 2025	October 01, 2026	January 01, 2027	October 01, 2028
ceramic block	Air-dry condition	1.83	1.86	1.86	1.86
	5 %	5.02	2.34	1.95	1.88
	8 %	8.05	2.70	2.02	1.89
	12 %	12.19	2.93	2.06	1.90
	Saturation state	128.33	5.50	2.49	1.97
mortar	Air-dry condition	1.37	1.35	1.34	1.34
	5 %	1.37	1.50	1.37	1.35
	8 %	1.37	1.59	1.40	1.35
	12 %	1,37	1.64	1.41	1.36
	Saturation state	1,37	1.98	1.49	1.37
adhesive	Air-dry condition	0.60	0.42	0.42	0.42
	5 %	0.60	0.43	0.42	0.42
	8 %	0.60	0.44	0.42	0.42
	12 %	0.60	0.44	0.42	0.42
	Saturation state	0,60	0.48	0.43	0.42
gypsum board	Air-dry condition	0.74	0.42	0.42	0.41
	5 %	0.74	0.42	0.42	0.41
	8 %	0.74	0.42	0.42	0.41
	12 %	0.74	0.43	0.42	0.41
	Saturation state	0.74	0.45	0.42	0.42

Table 6
Moisture content changes for the wall system made of silicate block.

Components of the wall system	Initial moisture content	Moisture content during the measurement period [%]			
		October 01, 2025	October 01, 2026	January 01, 2027	October 01, 2028
silicate block	Air-dry condition	1.50	1.31	1.29	1.28
	5 %	4.97	1.57	1.32	1.29
	8 %	7.98	1.73	1.33	1.28
	12 %	11.97	1.92	1.35	1.29
	Saturation state	19.13	3.34	1.45	1.28
mortar	Air-dry condition	1.37	1.22	1.20	1.20
	5 %	1.37	1.37	1.22	1.20
	8 %	1.37	1.46	1.23	1.20
	12 %	1,37	1.56	1.24	1.20
	Saturation state	1,37	2.21	1.32	1.21
adhesive	Air-dry condition	0.60	0.53	0.52	0.52
	5 %	0.60	0.54	0.53	0.52
	8 %	0.60	0.55	0.53	0.52
	12 %	0.60	0.56	0.53	0.52
	Saturation state	0,60	0.69	0.54	0.53
gypsum board	Air-dry condition	0.74	0.52	0.52	0.52
	5 %	0.74	0.53	0.52	0.52
	8 %	0.74	0.54	0.52	0.52
	12 %	0.74	0.55	0.52	0.52
	Saturation state	0.74	0.61	0.53	0.52

Table 7
Moisture content changes for the wall system made of concrete block.

Components of the wall system	Initial moisture content	Moisture content during the measurement period [%]			
		October 01, 2025	October 01, 2026	January 01, 2027	October 01, 2028
concrete block	Air-dry condition	2.41	2.50	2.54	2.56
	5 %	5.00	3.41	2.96	2.74
	8 %	8.00	3.92	3.16	2.84
	Saturation state	8.18	3.93	3.16	2.84
mortar	Air-dry condition	1.37	1.44	1.47	1.49
	5 %	1.37	1.95	1.70	1.61
	8 %	1,37	2.17	1.79	1.65
	Saturation state	1,37	2.18	1.79	1.65
adhesive	Air-dry condition	0.60	0.53	0.53	0.53
	5 %	0.60	0.56	0.54	0.53
	12 %	0,60	0.62	0.55	0.54
	Saturation state	0,60	0.62	0.55	0.54
gypsum board	Air-dry condition	0.74	0.52	0.52	0.52
	5 %	0.74	0.57	0.53	0.53
	12 %	0.74	0.59	0.54	0.53
	Saturation state	0.74	0.59	0.54	0.53

moisture content is observed for the saturation state for concrete and silicates. This is due to their significantly lower porosity compared to other materials. After three years, the moisture content of the structural material does not reach the air-dry state; the exception is the silicate block wall (Figs. 8 and 9, Tables 4–7),

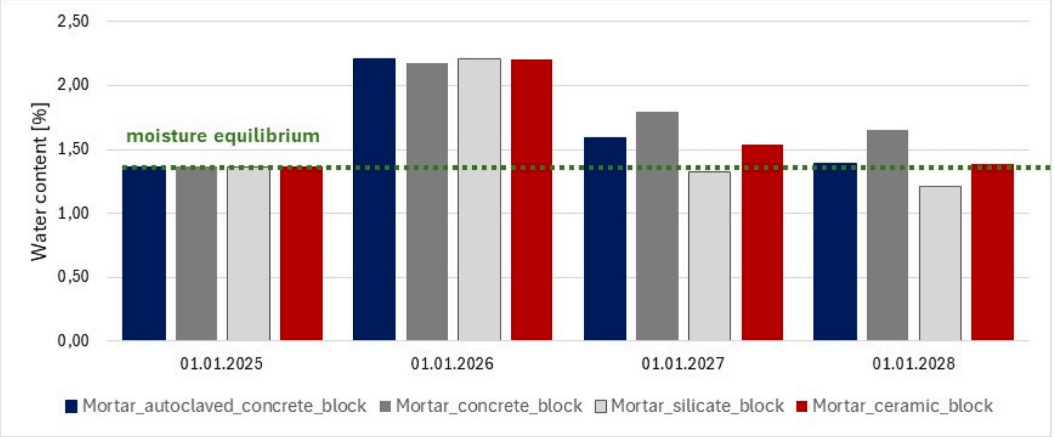

Fig. 9a. Moisture level in the mortar layer in subsequent calculation periods (variant V4).

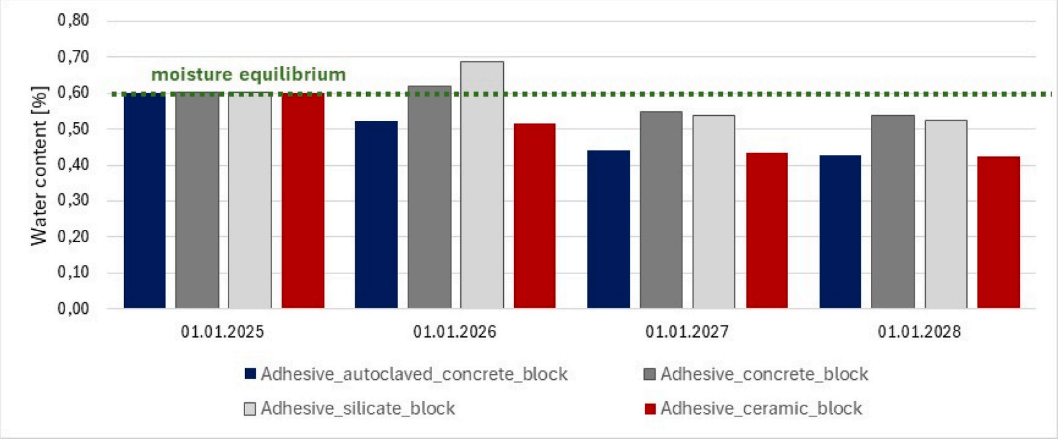

Fig. 9b. Moisture level in the adhesive layer in subsequent calculation periods (variant V4).

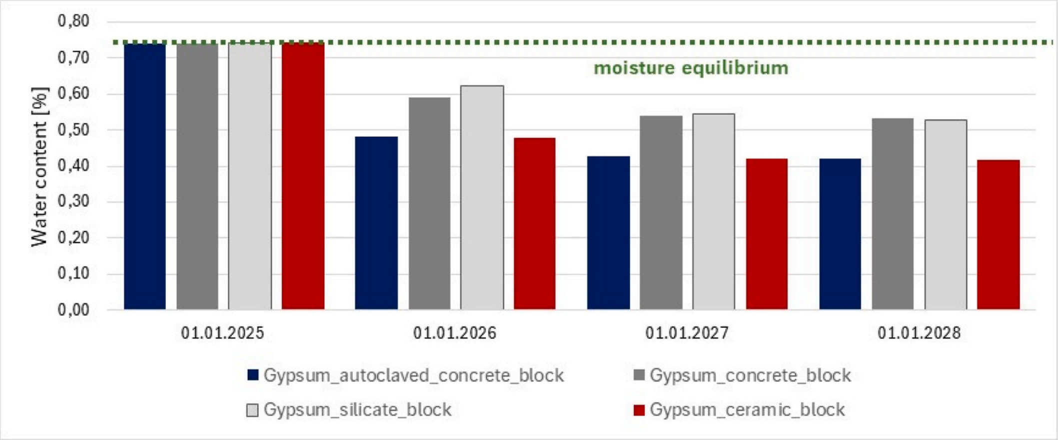

Fig. 9c. Moisture level in the gypsum board layer in subsequent calculation periods (variant V4).

- In the case of other layers of the system, i.e. mortar, adhesive, gypsum board, their moisture level is determined by the moisture content of the structural element (hollow block, block), i.e., despite the preset initial conditions for the air-dry state - in the initial phase there is an intensive increase in the moisture of these layers (visible especially for variants of the initial moisture of the structural material in the range of 8 % to state of saturation); nevertheless, already after 2 years, some of them dry down to the initial state, (e.g. adhesive, gypsum board), while for the rest, the drying period is at least 3 years (Figs. 8 and 9),
- Moisture in the internal layers of the wall, ie, the adhesive and gypsum board, is determined by the moisture content of the structural part only in the first calculation year. In the remaining period, sinusoidal changes in moisture content are observed, related to climatic conditions. This means that the moisture content decreases in

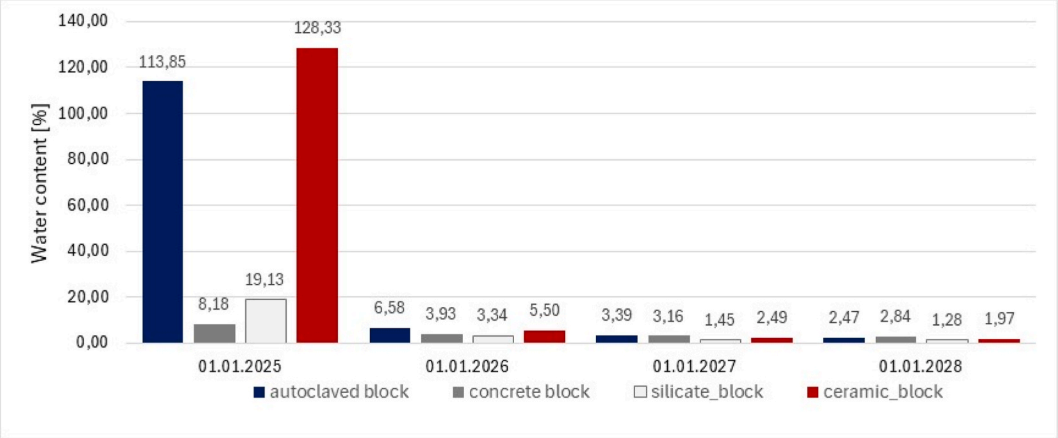

Fig. 9d. Moisture level in the structural layer in subsequent calculation periods (variant V4).

the winter season due to a decrease in relative humidity in the heated room (Figs. 8 and 9),

- A varied qualitative trend in moisture content is observed for the adhesive and gypsum board layers in the first year. However, in the second calculation year, regardless of the initial moisture level, the same qualitative and quantitative profile of changes in the moisture content is visible (Figs. 8 and 9),
- Calculations were conducted for the partition orientation toward the north (N), which is characterized by significantly less sunlight and is considered the least favorable for the partition's drying process.

The inner surface of a building component may be susceptible to mold growth if sufficiently high humidity and temperature conditions are provided. DIN 4108 specifies a critical value of 80 % RH on the surface. This value refers to the risk of mold growth on thermal bridges in winter, i.e., 12.6 °C (this is the surface temperature at which the assumed indoor air conditions of 20 °C and 50 % RH result in a critical surface humidity of 80 %). At higher temperatures, especially in summer, a surface humidity of around 75 % will be sufficient to allow mold to grow.

WUFIGraph include temperature-moisture diagrams, showing the computed relative humidity plotted against the corresponding temperature for each calculational time step. Different regions in such a diagram also represent different growth conditions for mold fungi, as far as these growth conditions are determined by the moisture and temperature conditions [15].

The temperature-humidity graph (Fig. 9) shows boundary curves indicating the minimum growth conditions characteristic of nutrient supply, typically found in building materials (boundary curves LIM B I and LIM B II). Designations of the curves: LIM I: biologically useable/organic substrate; LIM II: substrates with porous structure.

If temperature and humidity remain below these curves, mold growth is usually not expected. However, if the limit curves are exceeded for an extended period of time - the risk of mold growth depends on the duration and degree of mold-favorable conditions.

For the initial moisture conditions of the construction material (ranging from 5 % to the saturated state), based on the course of the isopleths (on the surface of the hollow block and gypsum board in contact with the air void – no mold growth is observed on the inner surface of the wall), it is observed that they exceed the limit curves indicating the minimum conditions for mold growth (Fig. 10 – limit curves LIM B I and LIM B II). Temperature and relative humidity remain above these curves during the initial period of operation, signaling a risk of mold growth. As the moisture content decreases over time, this risk becomes negligible. Nevertheless, due to the nature and initiating factors of mold development, the initial moisture state of the construction materials creates conditions conducive to microbial growth. It should be noted that the orientation of the partition, i.e. the north direction, also had an impact on the process of drying out the wall and the risk of mold development.

Fig. 11 shows the distributions of moisture content and temperature throughout the analyzed wall system on the final day of the calculation period (the x and y axes represent the model geometry – width and height, and the colored isolines represent the moisture level – the drawing is not to scale). The highest moisture levels are observed in the outer masonry layers, which is attributed to the influence of external climatic factors. These areas also exhibit the lowest temperatures at that time. In the partition model, significant quantitative differences are observed in the distribution of water across the thickness of the masonry and its individual layers. This finding provides justification for the recommendation that diagnostic studies of masonry—whether numerical or in situ—should assess moisture content across sections spanning the full transverse dimension.

3.3. *Prediction using GPR and accuracy of result approximation*

The training data were produced using WUFI 2D for four basic wall configurations (ceramic block, silicate block, autoclaved aerated concrete, and regular concrete), at six different initial moisture levels, using hourly climate data for Warsaw over a 3-year period (totaling 26,280 time steps). The simulations included external weather conditions (temperature, humidity, rainfall, solar radiation) and internal climate per PN-EN 15026 [42]. Although not directly prescribed, convective heat and moisture transfer coefficients used in the WUFI model implicitly account for local wind and pressure effects through calibrated surface resistances based on standard climatic datasets for Central Europe.

Each simulation produced a large spatio-temporal dataset, necessitating dimensionality reduction via PCA. Fig. 12 shows how much of the total variance is captured by a limited number of principal components. In most cases, 10 components retained over 95 % of the information, greatly simplifying further modeling.

The input to the Gaussian Process Regression model included.

- material properties (e.g., vapor resistance, porosity, thermal conductivity),
- initial moisture content [kg/m^3],
- geometric features (e.g., wall layer thicknesses),
- and compressed climate data (first principal amplitudes from PCA).

The GPR model was trained to estimate the drying time, defined as the duration required to reach a near-equilibrium moisture level. A radial basis function (RBF) kernel with automatic hyperparameter tuning was used, allowing fast and accurate predictions with confidence

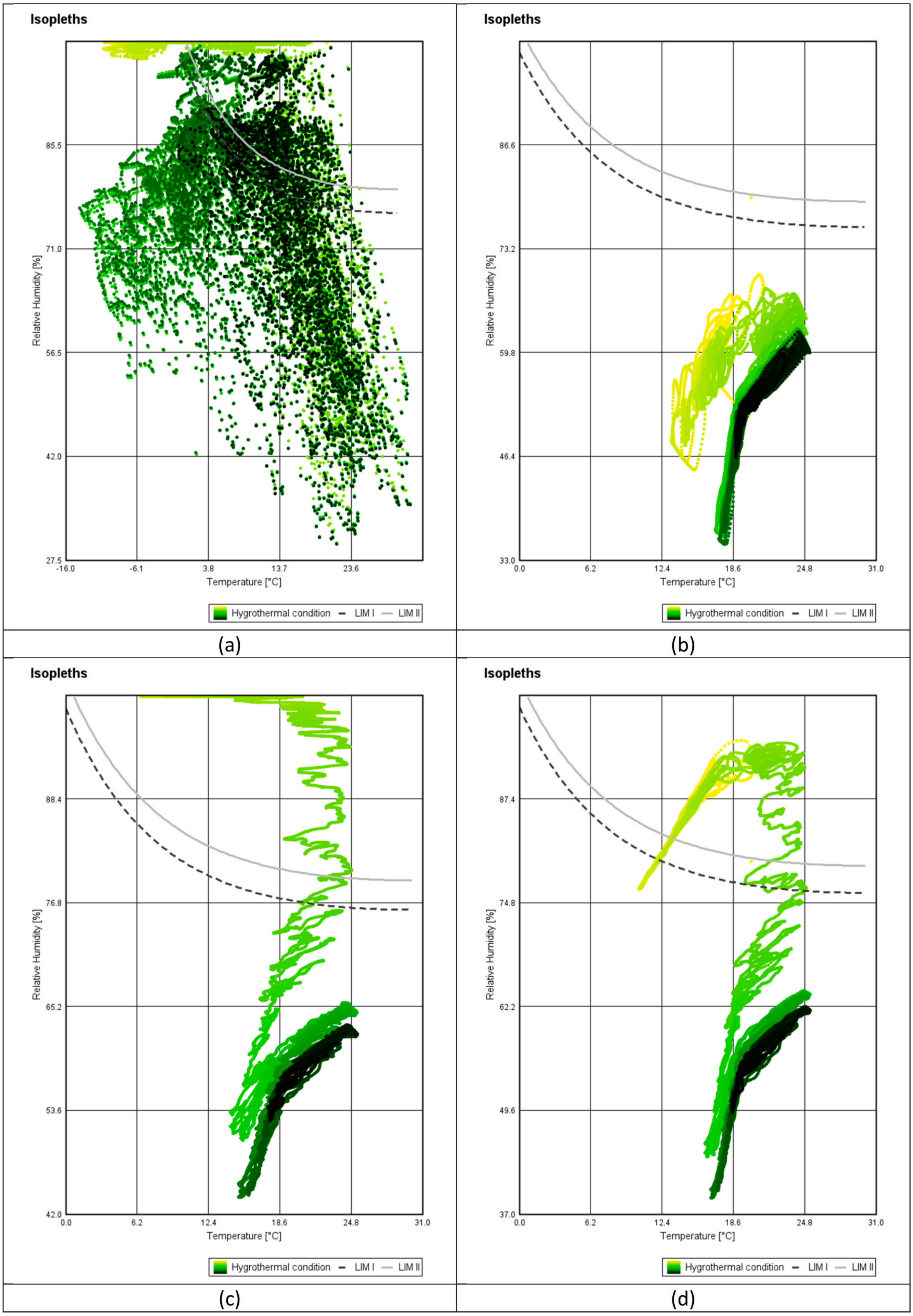

(a) (b)

(c) (d)

Fig. 10. Isopleth distribution profiles for the following surfaces: (a) external, (b) internal, (c) autoclaved aerated concrete block, (d) gypsum board (in contact with the air cavity) (for measured values). Color explanations: yellow – start, green – middle, end – black.

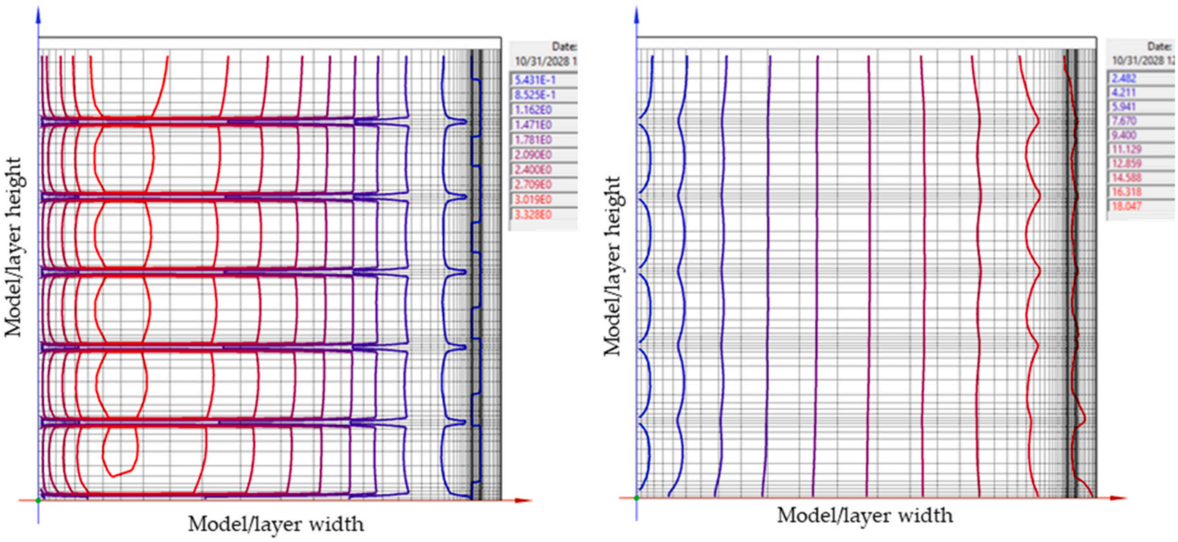

(a) (b)

Fig. 11. Changes in water content (a) and temperature (b) distribution across the entire analyzed wall system made of autoclaved aerated concrete blocks (results for the fully saturated moisture condition).

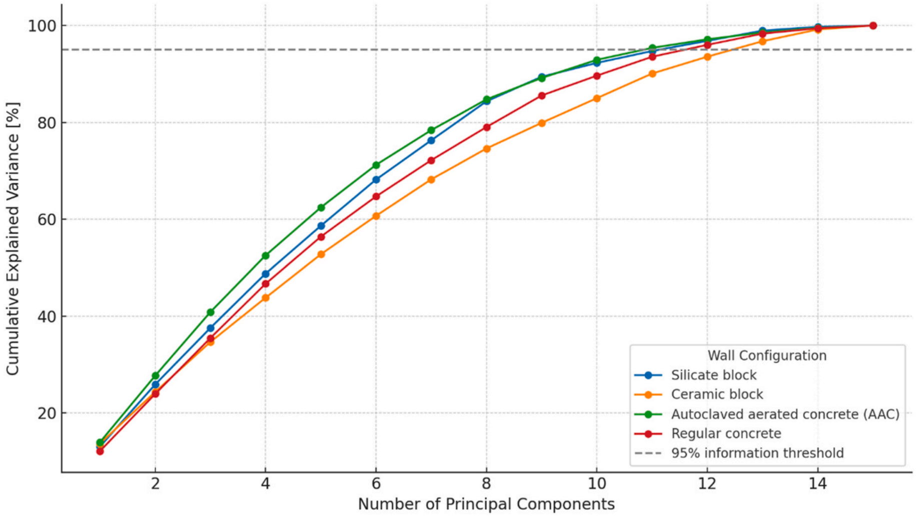

Fig. 12. Dimensionality reduction using PCA – variance retention.

intervals—critical for risk-aware engineering assessment.

Fig. 12 illustrates the percentage of cumulative variance explained by successive principal components for different wall configurations.

The results of the simulations clearly demonstrated the significant influence of material type, initial moisture content, and the layered structure of the wall on drying time. For the analyzed cases, the time required to reach a quasi-equilibrium moisture state ranged from several hundred to over 2000 days, depending on the configuration.

The shortest drying times were observed in walls made of silicate and autoclaved aerated concrete (AAC) blocks, which can be attributed to their high porosity and effective moisture redistribution capacity. In contrast, walls built with ceramic blocks and regular concrete dried much more slowly, particularly at higher initial moisture levels.

In non-structural layers (mortar, adhesive, and gypsum board), significant moisture accumulation was observed during the early stages of the simulation, even though air-dry conditions were assumed for those layers. This phenomenon resulted from moisture migration from the saturated structural components. After approximately 1.5–2 years—depending on the material and boundary conditions—some of these layers, particularly the adhesive and gypsum board, returned to their initial moisture states.

The surrogate model based on Principal Component Analysis (PCA) and Gaussian Process Regression (GPR) was able to accurately reproduce the results of full-scale simulations using only a limited number of principal components. As shown in the PCA analysis figure, as few as 10 principal components retained over 95 % of the system's variability in most cases, significantly reducing computational demands and making the approach practical for engineering use.

Moreover, the GPR model provides not only the expected drying time but also its confidence interval, which is essential for risk analysis and renovation planning. This enables fast comparison of material options and selection of moisture-optimized design solutions without the need for repeated full-scale numerical simulations.

To assess the quality of the GPR-based surrogate model, its predictions were compared with reference results obtained from detailed hygrothermal simulations conducted using WUFI 2D. The GPR model proved highly effective, achieving a coefficient of determination $R^2 = 0.988$, meaning it explained 96 % of the variability in the reference

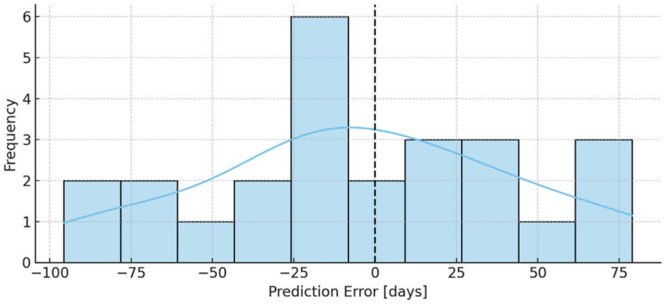

Fig. 13. Distribution of prediction errors (residuals).

data. The mean absolute error (MAE) was 38,76 days, and the root mean square error (RMSE) was 47,57 days (see Fig. 13).

Fig. 14 presents a comparison of the GPR-predicted values with those from WUFI simulations. Most data points lie close to the ideal agreement line, confirming the high accuracy of the predictions. The residuals histogram shows a symmetric distribution around zero, indicating no significant systematic bias.

The feature importance analysis (see Fig. 15) revealed that initial moisture content and porosity were the most influential factors in drying time prediction, followed by vapor resistance and dominant PCA climate components.

Table 8 shows 25 selected configurations, presenting reference values (from WUFI), GPR-predicted values, and absolute errors for each case. In long-term drying time prediction tasks, an absolute error of 5–10 % is generally considered acceptable depending on the material type and standard applied. In our case, most predictions fall within this range, with MAE = 47.1 days and RMSE = 51.3 days.

4. Conclusions

To build a reliable knowledge base for modeling and forecasting the drying behavior of water-damaged walls and for use in numerical simulations, extensive data collection is required to define the actual operational parameters of moisture-exposed building materials.

The study demonstrated that the drying process of multilayer wall assemblies depends significantly on the type of material, initial moisture content, and wall structure. Studies have confirmed scientific hypotheses that porous materials containing large pores as well as fine ones transport moisture well. Unprotected masonry (without a protective layer such as plaster) with prolonged (at least 24 h) exposure to water can reach a saturated state. As the research showed, the zone near the surface of the walls was the most damp. The highest rate of moisture loss

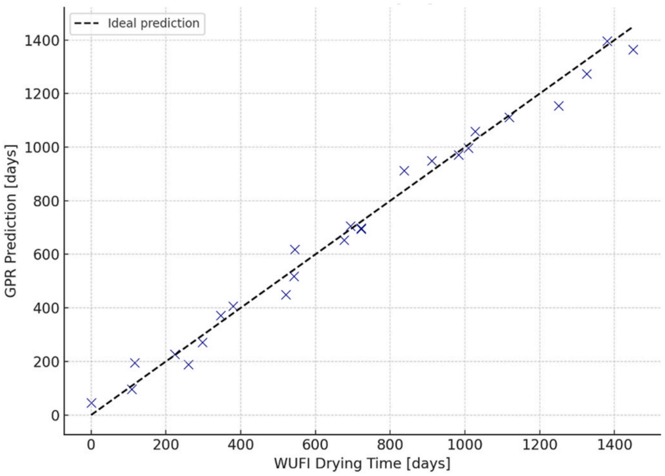

Fig. 14. GPR Model vs WUFI 2D – drying time prediction.

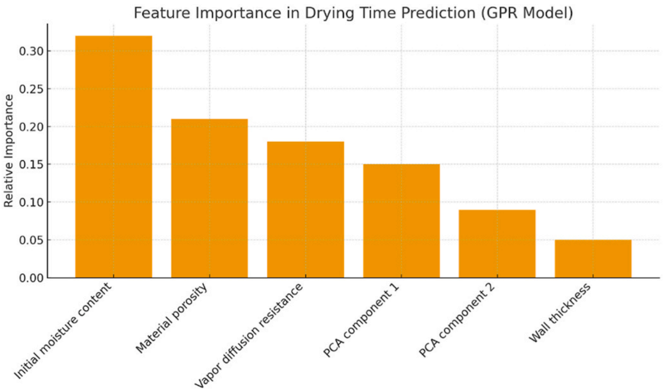

Fig. 15. Feature importance in drying time prediction (GPR model).

Table 8
Comparison of drying time predictions from the GPR surrogate model with reference values obtained from WUFI simulations.

	WUFI Drying Time [days]	GPR Prediction [days]	Absolute Error [days]
aerated concrete (air-dry condition)	347	371.8	24.8
aerated concrete (saturation state)	1118	1111.1	6.9
aerated concrete (measurement)	1027	1059.4	32.4
aerated concrete (3 %)		898.1	±47.6
aerated concrete (5 %)	837	913.2	76.2
aerated concrete (8 %)	983	971.3	11.7
aerated concrete (12 %)	1009	997.3	11.7
ceramic hollow blocks (air-dry condition)	116	195	79
ceramic hollow blocks (saturation state)	911	949.4	38.4
ceramic hollow blocks (measurement)	722	698.5	23.5
ceramic hollow blocks (3 %)	379	406.1	27.1
ceramic hollow blocks (5 %)	542	518.8	23.2
ceramic hollow blocks (8 %)	677	653.7	23.3
ceramic hollow blocks (12 %)	694	706.1	12.1
concrete blocks (air-dry condition)	1250	1154.3	95.7
concrete blocks (saturation state)	1450	1363.8	86.2
concrete blocks (measurement)	722	693.9	28.1
concrete blocks (3 %)		1193.5	±60.8
concrete blocks (5 %)	1325	1274.4	50.6
concrete blocks (8 %)	1380	1395.7	15.7
concrete blocks (12 %)		1557.4	±23.7
calcium silicate bricks (air-dry condition)	0	45.4	45.4
calcium silicate bricks (saturation state)	521	450.4	70.6
calcium silicate bricks (measurement)	545	618.3	73.3
calcium silicate bricks (3 %)	108	96.7	11.3
calcium silicate bricks (5 %)	223	226.4	3.4
calcium silicate bricks (8 %)	260	188.8	71.2
calcium silicate bricks (12 %)	298	270.8	27.2

*the red-colored values – these correspond to extrapolated predictions based on the GPR surrogate model in cases where the air-dry condition was not reached within the 3-year simulation period.

occurred during the first year, regardless of the initial saturation level. Tests conducted after a period of 6 months using the destructive method in the case of AAC showed moisture levels close to the near-surface zone, which may indicate the most uniform distribution of moisture in the horizontal section of the masonry. For other materials, moisture at a depth of about ½ the thickness of the masonry was less than in the near-surface layer. The wall models made of AAC, which underwent flooding and dried naturally after a period of 6mc, can be described according to the moisture criteria given as wet, while for the rest of the materials the degree of moisture in the masonry can be classified as acceptable moisture or increased moisture. However, after three years, most structural materials had not returned to air-dry conditions, with the exception of the silicate block wall. Non-structural layers such as mortar, adhesive, and gypsum board exhibited early moisture accumulation due to capillary transport from saturated cores, even though they were initially assumed to be dry. While some layers—like adhesive and gypsum board—returned to near-initial conditions after two years, others required a longer period to stabilize.

The results also showed that, under high initial moisture conditions, temperature and relative humidity levels on internal and external surfaces of the wall often exceeded critical thresholds for mold growth. Although this risk diminished over time due to drying, the early-stage conditions favored microbial development and should be considered during renovation planning.

To address the computational cost of simulating these phenomena in detail, a surrogate model was developed using Principal Component Analysis (PCA) and Gaussian Process Regression (GPR). This approach proved capable of accurately predicting drying time while significantly reducing computational demand. With just ten PCA components, over 95 % of the original moisture dynamics could be retained. The GPR model achieved a coefficient of determination of $R^2 = 0.988$, with a mean absolute error under 39 days, and offered valuable uncertainty estimates alongside each prediction.

The combination of material, climatic, and geometric data within a single surrogate model enables efficient evaluation of drying behavior under various conditions. This makes the approach highly applicable in engineering practice—particularly for design, diagnostics, and post-flood risk assessment. The model can generate predictions in a fraction of a second, whereas full numerical simulations in WUFI may take several hours per case. As such, the surrogate model provides an effective, practical alternative for large-scale or time-sensitive analyses. The surrogate model, trained on WUFI simulations for Warsaw's climate, is applicable to materials and configurations within the studied parameter space. Extension to other climatic zones or highly hygroscopic or hydrophobic materials would require re-training or additional calibration using local weather data and validated input parameters.

The key strength of the proposed approach lies in its ability to deliver accurate drying time predictions within a fraction of a second, without sacrificing detail or realism. This represents a major advancement over traditional tools such as the Glaser method or empirical lookup tables, which offer only rough, often non-conservative estimates. Furthermore, by integrating climate variability through PCA and providing predictive uncertainty via GPR, the model enhances usability in design and renovation scenarios, especially under limited data or time constraints.

CRediT authorship contribution statement

Barbara Ksit: Writing – review & editing, Writing – original draft, Supervision, Methodology, Investigation, Data curation, Conceptualization. **Anna Szymczak-Graczyk:** Writing – review & editing, Writing – original draft, Supervision, Project administration, Methodology, Investigation, Funding acquisition, Formal analysis, Data curation, Conceptualization. **Bożena Orlik-Kożdoń:** Writing – review & editing, Writing – original draft, Visualization, Validation, Supervision, Software, Resources, Methodology, Data curation. **Tomasz Garbowski:** Writing – review & editing, Writing – original draft, Visualization, Validation, Supervision, Software, Resources, Methodology, Data curation.

Declaration of competing interest

The authors declare that they have no known competing financial interests or personal relationships that could have appeared to influence the work reported in this paper.

Data availability

Data will be made available on request.

References

[1] Zhai ZJ, Helman JM. Implications of climate changes to building energy and design. Sustain Cities Soc 2019;44:511–9.
[2] Dino IG, Akgül CM. Impact of climate change on the existing residential building stock in Turkey: an analysis on energy use, greenhouse gas emissions and occupant comfort. Renew Energy 2019;141:828–46. https://doi.org/10.1016/j.renene.2019.03.150.
[3] Wan KK, Li DH, Pan W, Lam JC. Impact of climate change on building energy use in different climate zones and mitigation and adaptation implications. Appl Energy 2012;97:274–82. https://doi.org/10.1016/j.apenergy.2011.11.048.
[4] Ciancio V, Salata F, Falasca S, Curci G, Golasi I, de Wilde P. Energy demands of buildings in the framework of climate change: an investigation across Europe. Sustain Cities Soc 2020;60:102213. https://doi.org/10.1016/j.scs.2020.102213.
[5] Ksit B, Szymczak-Graczyk A. Diagnostics and multi-criteria analysis of methods for drying buildings after flooding. Case study. Civil and environmental engineering reports. CEER (Chem Econ Eng Rev) 2024;34(3):246–60. https://doi.org/10.59440/ceer/1920272024.
[6] Ksit B, Szymczak-Graczyk A, Pilch R. Numerical simulation of the impact of water vapour and moisture blockers in energy diagnostics of ventilated partitions. Materials 2022;15(22):8257. https://doi.org/10.3390/ma15228257.
[7] Bobociński A. Wpływ wilgotności ponadsorpcyjnej na przewodność cieplną betonów komórkowych [influence of over sorption moisture content on thermal conductivity of cellular concretes]. Build Res Inst 2004;4(132):3–12.
[8] Orlik-Kożdoń B. Microclimate conditions in rooms: their impact on mold development in buildings. Energies 2020;13:4492. https://doi.org/10.3390/en13174492.
[9] Garbowski T, Pawlak T, Szymczak-Graczyk A. Efficient load-bearing capacity assessment of a degraded concrete manhole using sectional homogenization. Materials 2024;17:5883. https://doi.org/10.3390/ma17235883.
[10] Pawlak T, Szymczak-Graczyk A, Garbowski T. Three-layer repair coating system for manholes, pump stations, and tanks in aggressive sulfate environment. Civil and environmental engineering reports. CEER (Chem Econ Eng Rev) 2025;35(1):1–19. https://doi.org/10.59440/ceer/196751.
[11] DIN 4108-3:2024-03. Izolacje cieplne i oszczędność energii w budynkach, część 3: ochrona przed wilgocią w zależności od warunków klimatycznych, wymagania, metoda obliczeń oraz wskazówki dotyczące projektowania i wykonawstwa. [Thermal protection and energy economy in buildings - Part 3: Protection against moisture subject to climate conditions - Requirements, calculation methods and directions for planning and construction].
[12] Smoczyk M, Ksit B, Szymczak-Graczyk A. Numerical analysis of the ground temperature function depending on edge thermal insulation parameters for shallow slab foundations. Energy 2025;314:134221. https://doi.org/10.1016/j.energy.2024.134221.
[13] Jin X, Zhang X, Cao Y, Wang G. Thermal performance evaluation of the wall using heat flux time lag and decrement factor. Energy Build 2012;47:369–74. https://doi.org/10.1016/j.enbuild.2011.12.010.
[14] Larsen SF, Filippín C, Lesino G. Thermal behavior of building walls in summer: Comparison of available analytical methods and experimental results for a case study. Build Simulat 2009;2:3–18. https://doi.org/10.1007/S12273-009-9103-6.
[15] https://wufi.de.
[16] Mavromatidis LE, El Mankibi M, Michel P, Santamouris M. Numerical estimation of time lags and decrement factors for wall complexes including multilayer thermal insulation, in two different climatic zones. Appl Energy 2012;92:480–91. https://doi.org/10.1016/j.apenergy.2011.10.007.
[17] Asan H, Sancaktar YS. Effects of wall's thermophysical properties on time lag and decrement factor. Energy Build 1998;28:159–66. https://doi.org/10.1016/S0378-7788(98)00007-3.
[18] Aste N, Angelotti A, Buzzetti M. The influence of the external walls thermal inertia on the energy performance of well insulated buildings. Energy Build 2009;41:1181–7. https://doi.org/10.1016/j.enbuild.2009.06.005.
[19] Quagraine KA, Ramde EW, Fiagbe YAK, Quansah DA. Evaluation of time lag and decrement factor of walls in a hot humid tropical climate. Therm Sci Eng Prog 2020;20:100758. https://doi.org/10.1016/j.tsep.2020.100758.
[20] Fathipour R, Hadidi A. Analytical solution for the study of time lag and decrement factor for building walls in climate of Iran. Energy 2017;134:167–80. https://doi.org/10.1016/j.energy.2017.06.009.
[21] Asadi I, Hashemi M, Sajadi B, Mahyuddin NB, Baghban MH, Esfandiari M, Maghfouri M, Yan K. Evaluating the time lag and decrement factor of mortar and

concrete containing OPBC as an agricultural By-Product lightweight aggregate. Case Stud Therm Eng 2023;41:102609. https://doi.org/10.1016/j.csite.2022.102609.

[22] Toure PM, Dieye Y, Gueye PM, Sambou V, Bodian S, Tiguampo S. Experimental determination of time lag and decrement factor. Case Stud Constr Mater 2019;11:e00298. https://doi.org/10.1016/j.cscm.2019.e00298.

[23] Belarbi YE, Ferroukhi MY, Issaadi N, Poullain P, Bonnet S. Assessment of hygrothermal performance of raw Earth envelope at overall building scale. Energy Build 2024;310:114119. https://doi.org/10.1016/j.enbuild.2024.114119.

[24] Luikov AV. Heat and mass transfer in capillary-porous bodies. In: Irvine TF, Hartnett JP, editors. Advances in heat transfer, vol. 1. Elsevier; 1964. p. 123–84.

[25] Adamski M, Czechlowski M, Durczak K, Garbowski T. Determination of the concentration of propionic acid in an aqueous solution by POD-GP model and spectroscopy. Energies 2021;14(24):8288. https://doi.org/10.3390/en14248288.

[26] Garbowski T, Cocchetti G, Cornaggia A, Ferrari R, Rizzi E. Inverse analysis investigation by gaussian processes optimisation of a historical concrete bridge relying on dynamic modal measurements. Eccomass Proceedia 2023:4249–64. https://doi.org/10.7712/120123.10716.21212.

[27] Buljak V, Garbowski T. Efficient methods for optimal space filling in model reduction techniques. In: Łodygowski T, Rakowski J, Litewka P, editors. Proceedings of XX international conference on computer methods in mechanics CMM2013, recent advances in computational mechanics. CRC Press; 2014. p. 285–92.

[28] Buljak V. Inverse analyses with model reduction. In: Computational fluid and solid mechanics. Springer Berlin Heidelberg; 2012. https://doi.org/10.1007/978-3-642-22703-5.

[29] Garbowski T. Stochastic model reduction applied to inverse analysis. In: Moitinho de Almeida JP, Díez P, Tiago C, Parés N, editors. Proceedings of the VI international conference on adaptive modeling and simulation ADMOS 2013. Barcelona: CIMNE; 2013. p. 291–300.

[30] Kubik J, Wyrwał J. Podstawy fizyki materiałów budowlanych [fundamentals of building materials physics]. In: Budownictwo ogólne [general construction], 2, Fizyka budowli. Warszawa; 2005. p. 9–52 [Building physics], P. Klemm.

[31] Pogorzelski JA. Zagadnienia cieplno-wilgotnościowe przegród budowlanych [thermal and moisture issues of building partitions]. Budownictwo ogólne [general construction], vol. 2; 2005. Fizyka budowli [Building physics], Warszawa.

[32] Wójcik R, Tunkiewicz M. Pory butelkowe – Charakterystyka, sposoby wyznaczania na przykładzie zaprawy cementowo-wapiennej [Ink-bottle pores – characteristics, methods of determination on the basis of lime – cements mortar]. Materiały Budowlane 2017;10:57–9.

[33] Sing KSW. Reporting physisorption data for gas/solid systems with special reference to the determination of surface area and porosity (recommendations 1984). Pure Appl Chem 1985;57(4):603–19.

[34] Kamiński K. Applied masonry rising damp models incongruity with „in situ" and laboratory findings, w: AMCM'2008 analytical models and new concepts in concrete and masonry structures. 6th Int Conf 2008:357–8.

[35] Ksit B. Diagnostyka wilgotnościowa obiektów budowlanych. Metodyka procedury badań [moisture diagnostics of building structures. Methodology of the test procedure]. Wydawnictwo Politechniki Poznańskiej, Poznań 2023.

[36] Ö-Norm B3355 2017 Trockenlegung von feuchtemMauerwerk – bauwerksdiagnostik und Planungsgrundlage ..

[37] EMERSIDA. Summary report on existing methods against rising damp. D2.1 FINAL version 31.07. https://www.emerisda.eu/wp-content/uploads/2014/07/D-2_1.pdf; 2014.

[38] PN-EN 16682:2017-05 Konserwacja dziedzictwa kulturowego – metody pomiaru zawartości wilgoci lub wody w materiałach nieruchomego dziedzictwa kulturowego [Conservation of cultural heritage. Methods for measuring moisture or water content in immovable cultural heritage materials].

[39] Gawin D. Modelowanie sprzężonych zjawisk cieplno-wilgotnościowych w materiałach i elementach budowlanych [mathematical model of hydro-thermal phenomena in porous media considering air dissolved in water]. Zeszyty Naukowe, 853, Rozprawy Naukowe, 279, Wydawnictwo Politechniki Łódzkiej, Łódź 2000.

[40] Gawin D, Kossecka E. Program komputerowy WUFI i jego zastosowanie w analizach cieplno-wilgotnościowych przegród budowlanych [computer program WUFI and its application in thermal and moisture analyses of building partitions]. Politechnika Łódzka, Łódź 2007.

[41] Kuenzel H. Simultaneous heat and moisture transport in building components. One- and two-dimensional calculation using simple parameters. Fraunhofer IBP; 1995.

[42] PN-EN 15026:2008 Cieplno-wilgotnościowe właściwości użytkowe komponentów budowlanych i elementów budynku. Szacowanie przenoszenia wilgoci za pomocą symulacji komputerowej [Hygrothermal performance of building components and building elements - Assessment of moisture transfer by numerical simulation].

[43] ASHRAE 160-2021 criteria for moisture-control design analysis in buildings. American Society of Heating, Refrigerating and Air-Conditioning Engineers, Inc.

[44] PN-EN ISO 6946:2017-10 Komponenty budowlane i elementy budynku. Opór cieplny i współczynnik przenikania ciepła. Metoda obliczania [Building components and building elements - Thermal resistance and thermal transmittance - Calculation methods].

[45] WTA Merkblatt 4-11-16/D, Messung des Wassergehaltsbzw der Feuchte von mineralischen Baustoffen. Wissenschaftlich-Technische Arbeitsgemeinschaft für Bauwerkserhaltung und Denkmalpflegee.V. München; 2016.

[46] WTA Wissenschaftlich-Technische Arbeitsgemeinschaft für Bauwerkserhaltung und Denkmalpflege e. V, Merkblatt 4-11-16/D Messung des Wassergehalts bzw der Feuchte bei mineralischen Baustoffen, Monachium, publikacje WTA 2016.

[47] Weber J. Baudiagnose und Geräte. In: Weber J, editor. Bauwerksabdichtung in der Altbausanierung: verfahren und juristische Betrachtungsweise, Hrsg. Wiesbaden: V. Hafkesbrink; 2012. p. 99–135.

[48] TROTEC T610, Instrukcja producenta [manufacturer's manual], https://pl.trotec.com/produkty-i-usługi/serwis/pobieranie/instrukcje-obslugi/mierniki/wilgotnosc/instrukcja-obslugi-miernik-wilgotnosci-t610/.

[49] Piotrowski J. Pomiary, czujniki i metody pomiarowe wybranych wielkości fizycznych i składu chemicznego [Measurements, sensors and measurement methods of selected physical quantities and chemical composition]. Warszawa; 2009.

[50] Hoła J. Degradacja budynków zabytkowych wskutek nadmiernego zawilgocenia – wybrane problemy [the degradation of historic buildings due to excessive moisture – selected issues]. Budownictwo i Architektura 2018;17(1):133–48.

[51] Adamowski J. Metodyka badań zawilgoconych murów [methodology for testing soggy masonry]. Materiały Budowlane 2005;7:6–8.

[52] Trochonowicz M. Wilgoć w obiektach budowlanych. Problematyka badań wilgotnościowych [Moisture in buildings objects. Humidity testing problems]. Budownictwo i Architektura 2010;7:131–44.

[53] Jasieńko J, Matkowski Z. Zasolenie i zawilgocenie murów ceglanych w obiektach zabytkowych – Diagnostyka, metodyka badań, techniki rehabilitacji [salinity and dampness of brick masonry in historic buildings - diagnosis, research methodology, rehabilitation techniques]. Wiadomości Konserwatorskie 2003;14:43–8.

[54] Frössel F. Mauerwerkstrockenlegung und Kellersanierung. Stuttgart: Wenn das Haus nasseFüße hat; 2012.